# Numerical Simulation of Leading-Edge Vortex Flows

Donald P. Rizzetta* and Joseph S. Shang*
*Air Force Wright Aeronautical Laboratories, Wright-Patterson Air Force Base, Ohio*

**Steady flowfields describing respectively the distinguished structure for subsonic, sonic, and supersonic leading-edge flow about a thin delta wing at angle of attack in a supersonic freestream are calculated numerically. Solutions of the steady three-dimensional compressible laminar Navier-Stokes equations are obtained by time integration. Details of these solutions demonstrate that the essential physical behavior of such flows, including both primary and secondary vortex motions, has been simulated. For purposes of comparison, a corresponding inviscid numerical solution was generated for the case of a subsonic leading edge. It is shown that, although the secondary features are absent, the gross dominant characteristics of the flowfield have been reproduced by the Euler equations. Effects of turbulence are assessed by incorporating a simple closure model in the viscous computation. Comparison between the numerical solutions and experimental data is provided for all flow regimes.**

## Nomenclature

$c$ = speed of sound, $(\gamma RT)^{1/2}$
$C_L$ = lift coefficient,

$$(1/\text{area}) \times \int_0^{z_{LE}} \int_0^L (C_{p_l} - C_{p_u}) dx dz$$

$C_p$ = pressure coefficient, $2(p-p_\infty)/\rho_\infty u_\infty^2$
$E$ = total specific energy
$F,G,H$ = vector fluxes
$L$ = model length in axial direction
$M$ = Mach number
$p$ = pressure
$Pr$ = Prandtl number, 0.73 for air
$R$ = gas constant
$Re_L$ = freestream Reynolds number, $\rho_\infty u_\infty L/\mu_\infty$
$t$ = time
$t_f$ = final computational time
$t_{CH}$ = characteristic time, $L/u_\infty$
$T$ = temperature
$u,v,w$ = Cartesian velocity components in $x,y,z$ direction
$u_{1,2,3}$ = $u,v,w$
$U$ = vector of dependent mass-averaged variables
$x,y,z$ = Cartesian coordinates in axial, normal, and spanwise directions
$\alpha$ = angle of attack
$\beta$ = numerical damping coefficient
$\gamma$ = ratio of specific heats, 1.4 for air
$\delta$ = model thickness
$\Delta$ = finite difference step size
$\theta$ = leading-edge vertex angle
$\mu$ = molecular viscosity coefficient
$\nu_{1,2,3}$ = $\xi,\eta,\zeta$
$\xi,\eta,\zeta$ = transformed body-fitted coordinates
$\rho$ = density

*Subscripts*

aw = adiabatic wall value
LE = evaluated at wing leading edge
max = maximum value
min = minimum value
$n$ = normal value
$p$ = property of fluid particle
$T$ = total condition
$u,l$ = evaluated on wing upper or lower surface
$w$ = evaluated on the surface
$\infty$ = freestream value

Received May 8, 1984; presented as Paper 84-1544 at the AIAA 17th Fluid Dynamics, Plasmadynamics and Lasers Conference, Snowmass, CO, June 25-27, 1984; revision received March 21, 1985. This paper is declared a work of the U.S. Government and therefore is in the public domain.

*Aerospace Engineer. Associate Fellow AIAA.

## Introduction

FLOWFIELDS about slender delta wings of small aspect ratio with sharp leading edges at the angle of attack have fascinated aerodynamicists for many years. Such flows may be characterized by a three-dimensional inviscid-viscous interaction, the most striking feature of which is the appearance of a core of spiraling fluid formed by the rolling up of a vortex sheet that separates from the leading edge and lies above the wing upper surfaces. In the inboard portion of this vortex, the fluid is directed downward toward the wing and forms a flow along the surface that is directed outboard toward the leading edge. An adverse pressure gradient in the outboard region of the wing is produced by the expansion about the leading edge and can result in the separation of the boundary layer and thus the appearance of a secondary vortex. This complex fluid behavior is of fundamental scientific interest and also can be of significance in aircraft design applications. The highly nonlinear relationship between the angle of attack and the resultant lift makes performance assessment of aerospace vehicles employing delta wings difficult. In addition, as the vortical flow proceeds downstream, it may eventually experience sudden breakdown or persist far into the wake region where it can pose a potential hazard for following aircraft.

Many experimental investigations[1-5] have been conducted in order to elucidate the intricate fluid behavior commonly observed for leading-edge vortex flows. While much of the information emanating from such studies has been of a qualitative nature, the descriptive results provided by flow visualization techniques have led to a broad understanding of the fundamentals of such behavior. Traditional analytical and empirical analyses.[6-9] have achieved some success in predicitng the gross properties associated with these flowfields, but have been unable to describe their physical details completely. More recently, numerical computations have provided characteristics of the flow properties that were not covered in previous theoretical treatments. Potential formulations employing panel[10] or vortex lattice[11] methods have been able to compute surface pressure distributions with

reasonable accuracy. A number of results corresponding to solutions of the Euler[12-14] and Navier-Stokes equations[15-19] for delta wing configurations have also been generated and represent a considerable advancement in predictive capabilities. The present work simulates the steady laminar flowfield about a thin sharp-edged delta wing by numerical integration of the three-dimensional compressible Navier-Stokes equations. In particular, the distinguished behavior for subsonic, sonic, and supersonic leading-edge flow, which has been noted experimentally by Stanbrook and Squire[2] and Monnerie and Werle[3] among others, is considered. The configuration to be examined is depicted schematically in Fig. 1 and consists of a delta wing of length $L$ with the leading edge swept at an angle of 75 deg and a thickness ratio ($\delta/L$) of 0.05. This geometry has an aspect ratio of 1.07 and duplicates the model of Monnerie and Werle[3] that was used to generate experimental data covering a wide range of Mach numbers and angles of attack.

For the case of a subsonic leading edge, a Navier-Stokes solution for this same geometry was computed by Vigneron et al.[15] in which the flow was assumed to be conical. Although this solution appeared to predict the primary vortex structure correctly, it produced no evidence of the secondary features that had been observed experimentally. The current investigation was undertaken in order to resolve this discrepancy. In addition, for the subsonic leading-edge case, the Navier-Stokes result is compared with a corresponding inviscid numerical calculation. Effects of turbulence were assessed by incorporating a simple closure model in the viscous computation. Comparison with experimental data is made for all flow regimes.

## Governing Equations

The governing equations are taken to be the unsteady compressible three-dimensional Navier-Stokes equations in mass-averaged variables, which may be expressed notationally in the following chain-rule conservative form:

$$\frac{\partial U}{\partial t}+\left(\frac{\partial \xi}{\partial x},\frac{\partial \xi}{\partial y},\frac{\partial \xi}{\partial z}\right)\begin{bmatrix}\frac{\partial F}{\partial \xi}\\ \frac{\partial G}{\partial \xi}\\ \frac{\partial H}{\partial \xi}\end{bmatrix}+\left(\frac{\partial \eta}{\partial x},\frac{\partial \eta}{\partial y},\frac{\partial \eta}{\partial z}\right)\begin{bmatrix}\frac{\partial F}{\partial \eta}\\ \frac{\partial G}{\partial \eta}\\ \frac{\partial H}{\partial \eta}\end{bmatrix}+\left(\frac{\partial \zeta}{\partial x},\frac{\partial \zeta}{\partial y},\frac{\partial \zeta}{\partial z}\right)\begin{bmatrix}\frac{\partial F}{\partial \zeta}\\ \frac{\partial G}{\partial \zeta}\\ \frac{\partial H}{\partial \zeta}\end{bmatrix}=0 \tag{1}$$

where $x,y,z$ are the Cartesian coordinates in the axial, normal, and spanwise directions, respectively (see Fig. 1), $\xi,\eta,\zeta$ the corresponding transformed coordinates in a body-oriented system, and

$$U=\begin{bmatrix}\rho\\ \rho u\\ \rho v\\ \rho w\\ \rho E\end{bmatrix} \tag{2}$$

is the vector of dependent variables. $F$, $G$, and $H$ are the vector fluxes whose form is well known[20] and thus are omitted here for brevity. The Cartesian velocity components are given by $u$, $v$, and $w$, $\rho$ is the density, and $E$ is the total energy per unit mass. A complete description of the system is provided by the perfect-gas law,

$$p=\rho RT \tag{3}$$

and the Sutherland formula for the molecular viscosity coefficient $\mu$.

In addition to laminar viscous solutions, one Euler and one turbulent Navier-Stokes computation were performed for comparative purposes. The Euler result was obtained by omitting the viscous stress and heat flux contributions to the vector fluxes $F$, $G$, and $H$. The effects of turbulence were incorporated by assigning a turbulent Prandtl number of 0.9 and by augmenting the molecular viscosity coefficient according to a simple algebraic turbulence closure model. For this purpose, the two-layer turbulent viscosity coefficient formulation due to Baldwin and Lomax[21] was employed. In the region of the flowfield outboard of the wing surface, this model was slightly modified such that the inner length scale was based upon the distance from the wing leading edge in a radial sense.

Freestream values were specified as boundary conditions for all of the dependent variables at the upstream, outboard, upper, and lower computational boundaries, i.e., $U=U_\infty$. At the wing midspan, a plane of symmetry was imposed that

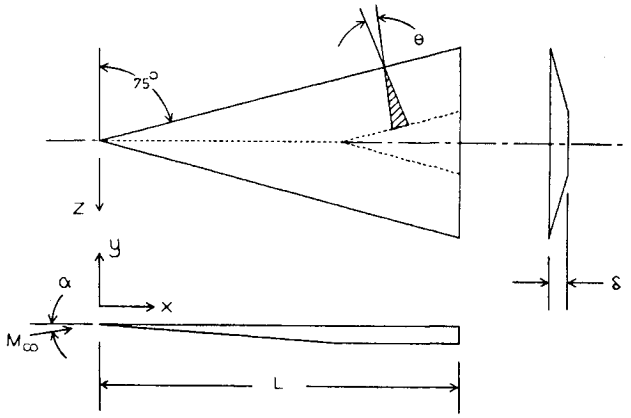


Fig. 1 Delta wing geometry.

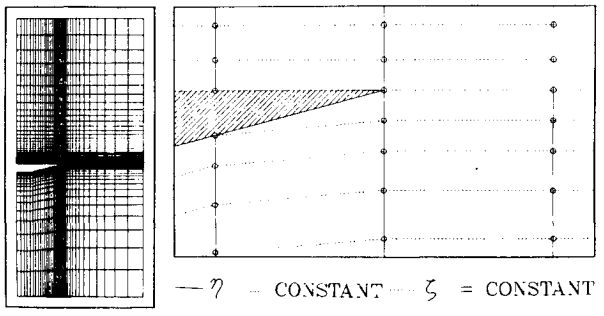


Fig. 2 Computational grid in $y$-$z$ plane at $x/L=1.0$.

resulted in

$$\frac{\partial \rho}{\partial \zeta} = \frac{\partial \rho u}{\partial \zeta} = \frac{\partial \rho v}{\partial \zeta} = \frac{\partial \rho E}{\partial \zeta} = w = 0 \text{ along } z = 0 \tag{4}$$

On the upper and lower wing surface,

$$u = v = w = 0 \tag{5a}$$

$$T = T_{aw} \tag{5b}$$

$$\frac{\partial p}{\partial \eta} = 0 \tag{5c}$$

for Navier-Stokes calculations and

$$u\frac{\partial \eta}{\partial x} + v\frac{\partial \eta}{\partial y} + w\frac{\partial \eta}{\partial z} = 0 \tag{6}$$

for the Euler solution. In the preceding, $T_{aw}$ is the adiabatic wall temperature and the left side of Eq. (6) constitutes the velocity component normal to the surface. Because computations corresponding only to supersonic freestream conditions were considered, no formal mathematical downstream boundary conditions were needed. However, due to the requirements of the numerical algorithm used to solve Eq. (1), values of the dependent variables at the downstream computational boundary were obtained by extrapolation from the interior domain.

## Numerical Procedure

Since the configuration is symmetric about the midspan, the numerical computations were performed about a half-span wing with a plane of symmetry situated at $z = 0$. For this purpose, a body-oriented nonorthogonal grid system consisting of $20 \times 64 \times 40$ points in the $\xi, \eta, \zeta$ directions was generated algebraically owing to the simplicity of the geometry involved. Due to application of supersonic freestream conditions, the forward boundary was located just upstream of the wing vertex. The first interior $y$-$z$ plane was chosen to lie at $x/L = 0.10$, which represents the minimum streamwise location where the wing spanwise dimension was sufficiently large to accommodate the $\xi$ distribution without excessive resolution. From this location, streamwise stations were taken in uniform increments of $x/L = 0.05$ up to the downstream boundary at $x/L = 1.0$. In $y$-$z$ planes, grid lines were exponentially stretched upward and downward away from the wing surface and inboard and outboard away from the leading edge. A description of the mesh spacing and computational boundaries employed at all $y$-$z$ planes for the cases to be considered is given in Table 1. Figure 2 illustrates the $y$-$z$ plane at $x/L = 1.0$ for the case $M_\infty = 1.95$, showing the detailed spacing at the wing leading edge. In this plane, it is noted that the mesh consists of an H-grid structure such that the transformed coordinate lines do not wrap around the sharp leading edge. The grid point indicated exactly at the leading edge is assumed to lie just outboard of the wing surface such that no ambiguity about the application of the surface boundary condition [Eq. (5c)] arises. For the higher Mach number cases, the outboard mesh boundary $z_{max}$ was varied linearly in $x$, incorporating a larger value of $z_{max}/z_{LE}$ upstream in order to capture the embedded shock wave properly. This grid system employs 40 of the $\eta$ grid lines on and above the wing surface and 24 of the $\xi$ grid lines inboard of the leading edge. All of the metric coefficients appearing in Eq. (1) are obtained numerically by second-order-accurate formulas corresponding to central differences at the interior mesh points and one-sided differences at the wing surface and computational boundaries.

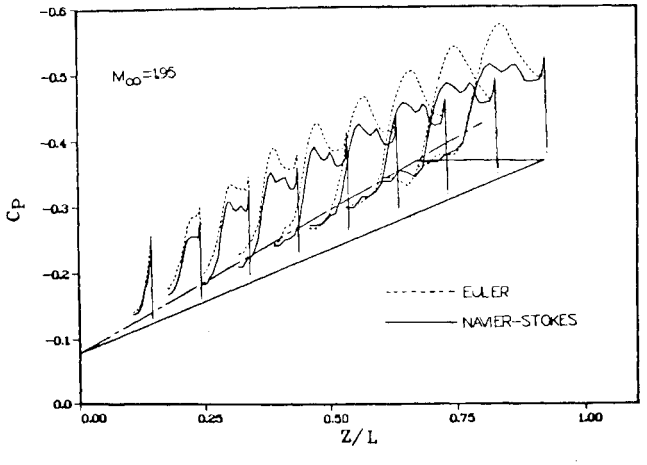


Fig. 3 Comparison of Euler and Navier-Stokes upper surface pressure distributions for $M_\infty = 1.95$.

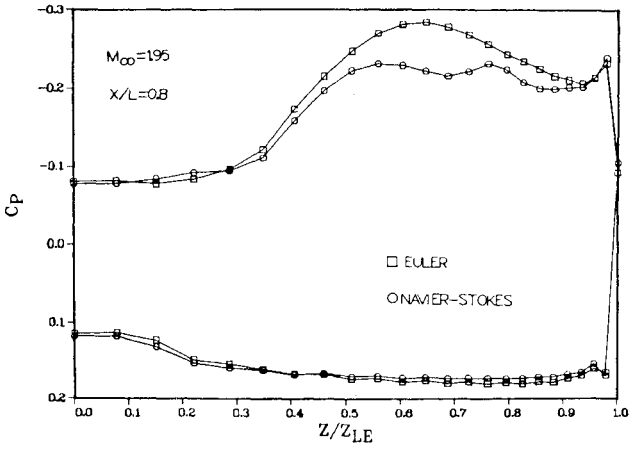


Fig. 4 Comparison of Euler and Navier-Stokes surface pressure distributions for $M_\infty = 1.95$ at $x/L = 0.8$.

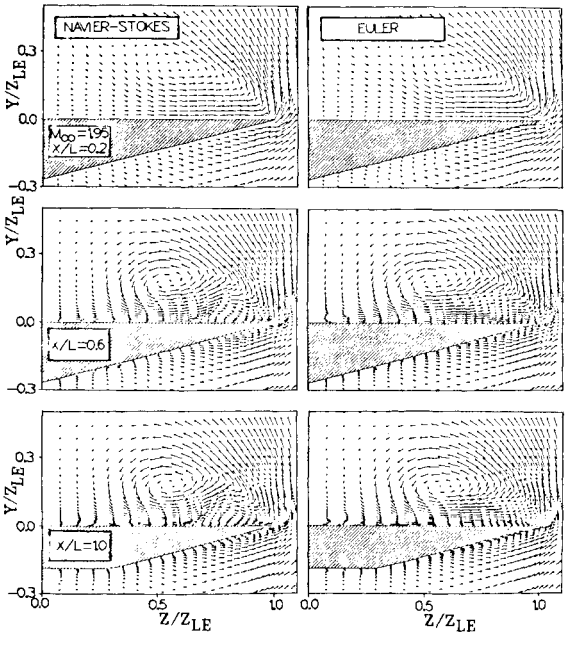


Fig. 5 Comparison of Euler and Navier-Stokes cross-plane velocity vectors for $M_\infty = 1.95$.

Surface values required by the algorithm for solution of the Euler equations were obtained by extrapolation of the density and energy from the interior domain. The tangential contravariant velocity components were also extrapolated in order to provide the following values at the surface:

$$\left(u\frac{\partial \xi}{\partial x}+v\frac{\partial \xi}{\partial y}+w\frac{\partial \xi}{\partial z}\right)_w = \text{extrapolated value} \quad (7a)$$

$$\left(u\frac{\partial \zeta}{\partial x}+v\frac{\partial \zeta}{\partial y}+w\frac{\partial \zeta}{\partial z}\right)_w = \text{extrapolated value} \quad (7b)$$

Equations (7) were then solved simultaneously with the boundary condition [Eq. (6)] in order to generate the necessary Cartesian velocity components. This procedure embodies the concept of analytic continuation in order to satisfy algorithmic requirements.

Steady-state solutions to Eq. (1) were generated using the well-established, time-dependent, explicit, unsplit two-step predictor-corrector finite difference algorithm of MacCormack[22] that has evolved as a reliable technique for the numerical solution of a wide variety of fluid dynamic problems. As part of this algorithm, a fourth-order pressure damping term,[23] commonly employed to suppress numerical oscillations arising from regions with large gradients in the dependent variables, was incorporated. The form of this term is given as

$$\beta\Delta t\sum_{j=1}^{3}(\Delta v_j)^3\frac{\partial}{\partial v_j}\left[\frac{\partial U}{\partial v_j}\left|\frac{\partial^2 p}{\partial v_j^2}\right|\frac{|u_j+c|}{p}\right] \quad (8a)$$

where

$$v_{1,2,3}=\xi,\eta,\zeta \text{ and } u_{1,2,3}=u,v,w \quad (8b)$$

which is then added to the new value of $U$ at each time step. All of the calculations were generated with the damping coefficient $\beta=2.0$. For the two lowest Mach number cases, damping in the normal direction ($\eta$) could be omitted without any observed numerical difficulties. Solutions with and without normal pressure damping were indistinguishable. In the case of $M_\infty=7.0$, a stable solution could not be obtained without normal pressure damping due to the strength of the shock wave present within the flowfield.

The initial conditions for all of the solutions were taken as freestream values at grid points inside the computational domain, except on the interior boundary where the surface conditions were invoked. The one exception to this procedure was the turbulent calculation which was initiated from a previously generated steady laminar solution. In order to remove the initial transients, the numerical flowfields were allowed to evolve for 100 time steps with $\Delta t$ chosen such that the maximum Courant number was 0.5. The solutions then proceeded to the steady state with a Courant number of 0.8. Again, the exception was the turbulent case which was unstable above a Courant number of 0.5, probably due to a higher shear stress near the surface than occurred in the laminar cases. The total physical time over which solutions were evolved ($t_f$) is provided in Table 1 in terms of the characteristic flow time $t_{CH}=L/u$. The behavior of these solutions was carefully monitored before they were declared to be converged. Contours of pressure and vorticity were observed, together with the cross-flow velocity, surface pressure, and absolute vorticity level. There were two reasons for allowing evolution times considered to be excessive: 1) the vortex structure emerged rather slowly, particularly at the downstream boundary; and 2) any possibility of nonconvergence could then be eliminated from consideration when examining the solutions. In most cases, practical results would be obtained in about one-third the evolution times quoted in Table 1.

All of the aforementioned features of the numerical algorithm are embodied in an efficient vectorized solver[20] written especially for the CRAY-1 computer, which has performed well for a number of three-dimensional calculations and was used to produce the results presented here. This solver advances the solution from one time step to the next in the $\eta$-$\zeta$ planes by marching in the $\xi$ direction, thus minimizing the data flow to and from central memory. Using the previously defined computational grid, approximately 730K decimal words of storage were required. A data processing rate of $7.7\times10^{-5}$ CPU s/time step/grid point was achieved for the Navier-Stokes computations and a rate of $5.5\times10^{-5}$ for Euler calculations where vectorization occurred in the $\zeta$-direction with a vector length of 40.

## Results

Numerical solutions were generated for flow about the delta wing shown in Fig. 1 at an angle of attack $\alpha=10$ deg for freestream Mach numbers of 1.95, 4.0, and 7.0. These conditions duplicate the experiments of Monnerie and Werle[3] and correspond to Mach numbers normal to the leading edge of 0.50, 1.02, and 1.78, respectively. Geometric parameters and test conditions of these experiments are summarized in Table 2. In addition to laminar Navier-Stokes calculations for all cases, an Euler solution was computed for $M_\infty=1.95$ and a turbulent solution obtained for $M_\infty=4.0$. It is considered to be significant that these results were generated using identical computational grids and by the same numerical code, such that algorithmic and discretization differences arising between the solutions were minimized.

Results for $M_\infty=1.95$ are presented in Fig. 3 in terms of the upper surface pressure distribution where both viscous and inviscid solutions are shown for comparison. It is seen that the Navier-Stokes result produces a generally larger value of the pressure coefficient on the upper surface due to the viscous displacement effect of the boundary layer (which is absent in the Euler solution). A more detailed comparison of these results appears in Fig. 4, where both the upper and lower surface pressure distributions are displayed for $x/L=0.8$. Although the fundamental behavior of the vortex flow is inherently three-dimensional, its physical character-

**Table 1 Computational parameters**

| $M_\infty$ | $\Delta y_{min}/L$ | $y_{min}/z_{LE}$ | $y_{max}/z_{LE}$ | $z_{max}/z_{LE}$ | $t_f/t_{CH}$ |
|---|---|---|---|---|---|
| 1.95 N-S (laminar) | $9.7971\times10^{-4}$ | −3.0 | 3.25 | 2.75 | 31.6 |
| 1.95 Euler | $9.7971\times10^{-4}$ | −3.0 | 3.25 | 2.75 | 11.3 |
| 4.0 N-S (laminar) | $7.8377\times10^{-4}$ | −2.0 | 3.0 | 2.0-4.0 | 18.5 |
| 4.0 N-S (turbulent) | $7.8377\times10^{-4}$ | −2.0 | 3.0 | 2.0-4.0 | 5.0 |
| 7.0 N-S (laminar) | $3.6576\times10^{-4}$ | −1.5 | 2.5 | 2.0-3.0 | 20.9 |

istics can be inferred from the two-dimensional Euler pressure distribution shown in Fig. 4. As the freestream flow encounters the wing surface, it expands over the leading edge, producing a local pressure minimum. Because the leading edge is sharp and the freestream velocity is low ($M_n = 0.50$), the flow separates from the wing surface, resulting in a slight recompression immediately inboard of the leading edge. The separated flow then forms into a spiraling vortex that entrains fluids from the region above the wing and creates subsequent acceleration of the flow. This can be observed in the pressure minimum at $z/z_{LE} \approx 0.65$ of the Euler solution. Inboard of the vortex, there is no acceleration due to entrainment and thus recompression to a uniform pressure along the centerline occurs.

The basic effect of viscosity on the pressure distribution is that of displacement, which is evident in the Navier-Stokes solution shown in Fig. 4. Viscous displacement reduces the turning of the inviscid flow, thereby reducing expansion and increasing the pressure level on the wing upper surface. For this case, there is also a viscous separation of the boundary layer that results in the formation of a secondary vortex near the wing surface. The viscous separation causes a "bump" to form in the displacement surface and produces a corresponding "bump" in the pressure distribution, which is seen to be located at $z/z_{LE} \approx 0.75$. These surface pressures resulted in computed lift coefficients of $C_L = 0.301$ for the Navier Stokes solution and $C_L = 0.321$ for the Euler solution.

Cross-plane velocity vector plots corresponding to these solutions are shown in Fig. 5. Upstream ($x/L = 0.2$), the evolution of the primary vortex appears to be predicted with similar characteristics by both sets of equations. This emphasizes the fact that formation of the primary vortex is inherently an inviscid phenomena. It is noted that the primary vortex induces a strong outboard-directed flow near the surface that persists even in the viscous case satisfying the no-slip condition. Further downstream ($x/L = 0.6, 1.0$), the viscous separation forming the secondary vortex appears as a

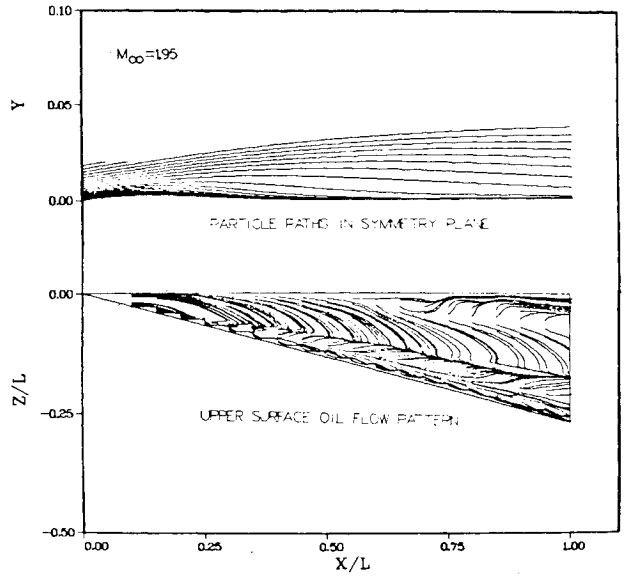


**Fig. 6 Particle paths in symmetry plane and upper surface oil flow pattern of Navier-Stokes solution for $M_\infty = 1.95$.**

**Table 2 Parameters for experiments of Monnerie and Werle[3]**

| $M_\infty$ | $\delta$,mm | $\theta$,deg | $L$,mm | $P_{T_\infty}$,kPa | $T_{T_\infty}$,K | $Re_{LE}$ |
|---|---|---|---|---|---|---|
| 1.95 | 3.5 | 15 | 70 | 100 | 288 | $9.5 \times 10^5$ |
| 4.0 | 3.5 | 15 | 70 | 500 | 310 | $2.5 \times 10^6$ |
| 7.0 | 8.0 | 20 | 150 | 6500 | 600 | $4.5 \times 10^6$ |

recirculating region in the cross plane. Comparison with the Euler solution indicates that the size and location of the primary vortex are only slightly modified by viscous separation. The prior solution of Vigneron et al.[15] for the same case showed no evidence of secondary features when the conical approximation to the Navier-Stokes equations was made. It is apparent from Figs. 3 and 5 that the flow structure cannot be considered conical as it evolves downstream.

For the case of a steady flow, the instantaneous rate of change of the position of a fluid particle is given by the fluid velocity vector, i.e.,

$$\frac{dx_p}{dt} = u, \quad \frac{dy_p}{dt} = v, \quad \frac{dz_p}{dt} = w \tag{9}$$

Equation (9) may be integrated over some arbitrary time interval in order to obtain the fluid particle path in the computational flowfield. In addition, if the $x$-$z$ grid plane lying immediately above the wing surface is considered and the normal velocity neglected, then the apparent oil surface flow diagram may be constructed. Results of this procedure appear in Fig. 6. The particle paths, which coincide with streamlines for the steady state, indicate expansion of the flow over the wing vertex and its subsequent recompression downstream. The computed oil flow pattern clearly exhibits the separation and reattachment of the secondary vortex, as well as the reattachment of the primary vortex just outboard of the plane of symmetry, and compares favorably with observed results. Secondary separation can be seen to occur for fluid traveling downstream and outboard from the primary reattachment line. This separation is provoked when the fluid encounters the adverse pressure gradient near the leading edge. Upstream, the spanwise dimension of the wing $z_{LE}$ is very short, such that the distance traversed from the reattachment line to the leading edge is also short. Along this path, the fluid loses momentum, but can still maintain attached flow. Further downstream, however, $z_{LE}$ is longer. Hence, the greater distance traversed results in a more substantial momentum loss and ultimately in separation. Formation of the secondary vortex appears to be predicted for $x/L \approx 0.4$.

The path of a typical fluid particle traversing the region above the wing surface is displayed in Fig. 7. For clarity, the projection of this path onto the wing surface, the plane of symmetry, and the downstream boundary are provided. Entering the computational domain at the upstream boundary, the particle flows upward over the wing surface following the expansion over the leading edge and is then swept downward and outboard. As it nears the leading edge, the vortical flow forces it upward and inboard. After making a complete revolution, the particle travels outboard again and upward until it reaches the downstream boundary.

For $M_\infty = 4.0$, both laminar and turbulent Navier-Stokes solutions were generated. The upper surface pressure distributions from these results are compared in Fig. 8, which indicates only minor differences between the two. Figure 9 shows the more detailed comparison of surface pressure at $x/L = 0.8$. It is seen that the most prominent differences between the two solutions occur on the lower surface and result in a lift coefficient that is approximately 5% higher in the turbulent case. The corresponding cross-plane velocity vector plots at this location are shown in Fig. 10. In this case, because the freestream velocity is higher and the leading edge sonic, there is no recompresssion of the flow following the turning over the leading edge. This results in a very uniform pressure distribution on the upper surface. The flow separates approximately at the leading edge and forms a primary vortex. This vortex is seen to be much smaller in extent and to lie further inboard than was the case for $M_\infty = 1.95$, a situation that occurs because the higher axial velocity inhibits rotation and thus entrainment as the vortex

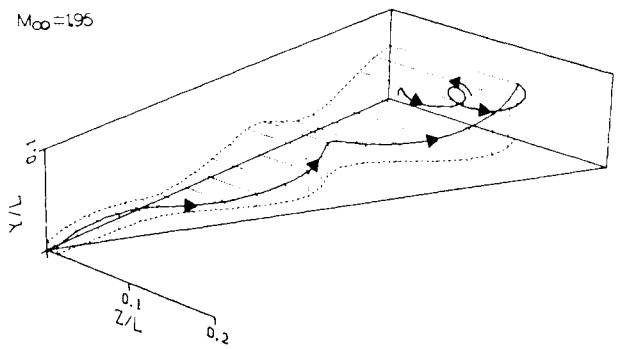


Fig. 7 Particle path of Navier-Stokes solution for $M_\infty = 1.95$.

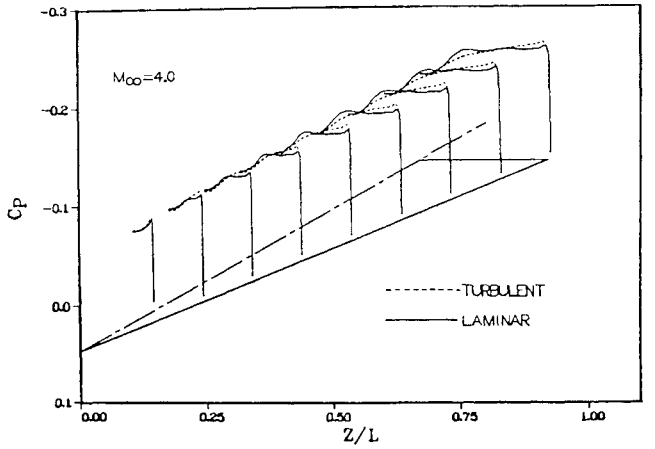


Fig. 8 Comparison of laminar and turbulent Navier-Stokes upper surface pressure distributions for $M_\infty = 4.0$.

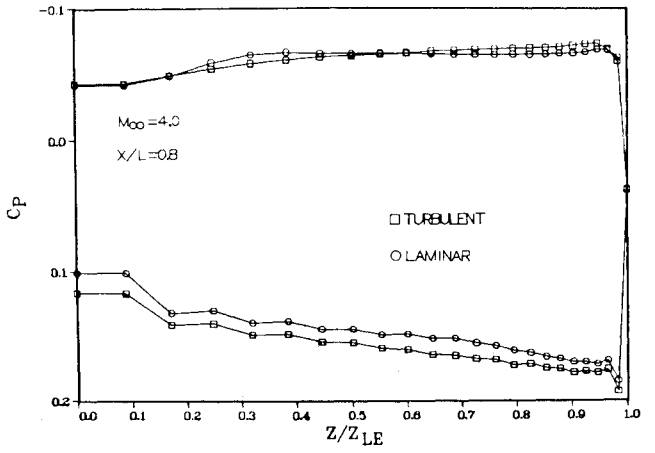


Fig. 9 Comparison of laminar and turbulent Navier-Stokes surface pressure distributions for $M_\infty = 4.0$ at $x/L = 0.8$.

spirals downstream. Inboard of the vortex, a slight recompression is evident in the pressure distribution (Fig. 9) where reattachment takes place. The lack of an adverse pressure gradient in the outboard region and the higher axial velocity preclude viscous separation and hence the formation of a secondary vortex. This is confirmed by the computed surface oil flow pattern (not shown here), as well as the velocity vector plot of Fig. 10.

Differences between the laminar and turbulent solutions appear to be minimal. On the upper surface, the strength of the vortex is seen to be reduced by turbulent viscosity in Fig. 10. It is also evident that the surface velocity profiles are much fuller in the turbulent case, as is to be expected. Numerical computation confirmed that the turbulent solution resulted in less viscous displacement than was present in the laminar case. Thus, the weakening of the vortex is offset by the reduction in displacement such that the upper surface pressure distribution is virtually the same for both calculations. On the lower surface, the turbulent computation also produced less viscous displacement. This results in more turning of the flow and explains the differences between the solutions observed in Fig. 9.

The surface pressure distribution for the laminar Navier-Stokes solution at $M_\infty = 7.0$ and $x/L = 0.8$ is presented in Fig. 11. Previous results for $M_\infty = 1.95$ and 4.0 are provided for comparison. In addition, the experimental results,[3] which were available only on the upper surface for $M_\infty = 4.0$ and 7.0 and $0.0 \le z/z_{LE} \le 0.9$, are also displayed. For $M_\infty = 7.0$, the leading edge is supersonic and therefore the upper and lower surface flowfields are independent. Separation is now found to occur inboard of the leading edge, as is apparent in the cross-plane velocity vector plot of Fig. 12, as well as in the corresponding oil surface flow pattern (not shown). The vortex is seen to be smaller in extent and lie even further inboard than was evident for $M_\infty = 4.0$. Thus, the effect of the vortex on the surface pressure is negligible and results in a nearly uniform distribution corresponding to that of the flow over a flat plate at the angle of attack with $M_\infty = 7.0$ ($C_p = -0.025$). Agreement with experimental data is quite good for both $M_\infty = 4.0$ and 7.0.

For the highest Mach number case, neither the experimental data nor the numerical solution give evidence of the cross-flow shocks commonly observed at higher angles of attack or higher freestream Mach numbers. The corresponding cross-plane Mach number contour plot (not shown) does indicate, however, that Mach lines are beginning to coalesce in the region above the vortex, which is consistent with the computations of Bluford,[16] where high Mach number flows were considered and cross-plane shocks observed. As was also true for $M_\infty = 4.0$, no secondary separation occurs because of the high axial velocity and the lack of an adverse pressure gradient. On the underside of the wing, the higher velocity produces more expansion where the flat bottom surface meets the bevel from the leading edge. This results in a lower and nearly uniform pressure along the flat portion of the surface near the plane of symmetry. In Fig. 12, the

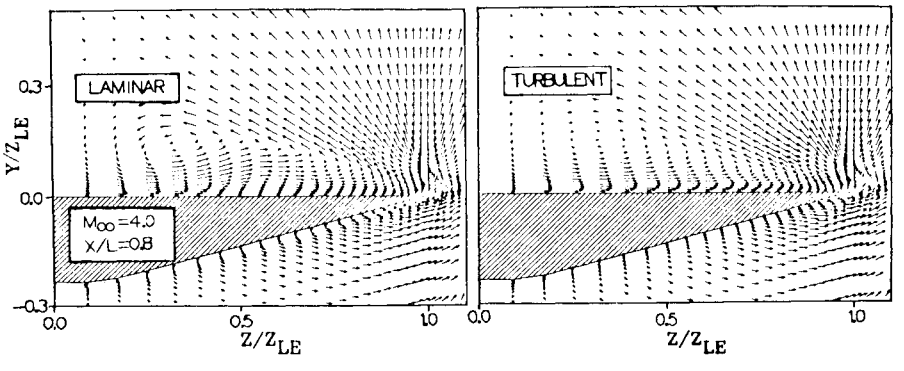


Fig. 10 Comparison of laminar and turbulent Navier-Stokes cross-plane velocity vectors for $M_\infty = 4.0$ at $x/L = 0.8$.

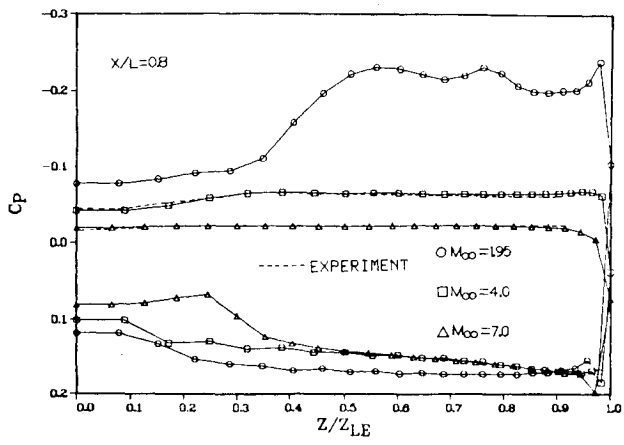


Fig. 11 Navier-Stokes surface pressure distributions at $x/L = 0.8$.

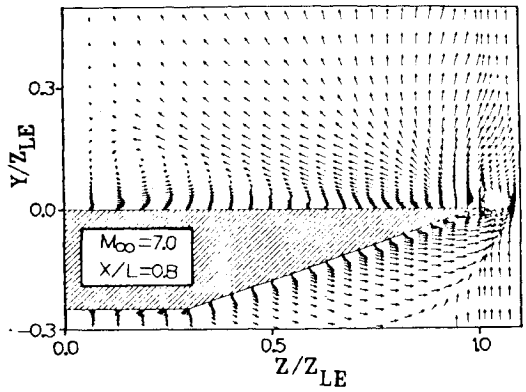


Fig. 12 Navier-Stokes cross-plane/velocity vectors for $M_\infty = 7.0$ at $x/L = 0.8$.

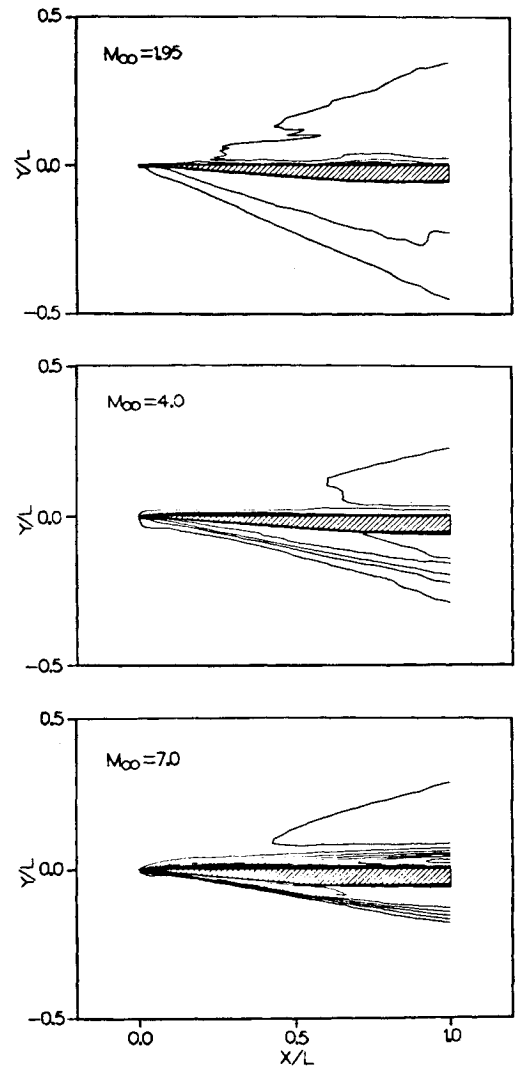


Fig. 13 Navier-Stokes Mach number contours in symmetry plane.

strong shock wave is apparent below the lower surface in the outboard region of the flowfield.

Mach number contours for all three cases are shown in Fig. 13. The extent of the flowfield affected by the presence of the wing is seen to decrease as the Mach number increases. On the upper surface, the effect of the expansion over the wing vertex and subsequent recompression downstream are evident. In the lower downstream portion of the flowfield, the change of surface geometry on the underwing surface can be seen to produce a weak expansion.

Figures 14-16 provide comparison of these computations with the experimental measurements of Monnerie and Werle[3] in terms of total pressure surveys taken above the wing upper surface at $x/L = 0.8$. The comparison for $M_\infty = 1.95$ is displayed in Fig. 14. The size and location of the primary vortex appear to agree reasonably well, although the comparison in the upper portion of the flowfield is not as favorable. In the region of secondary flow, the calculation seems to correlate well with the measured data. Total pressure contours from the Euler solution were virtually identical to those of the Navier-Stokes calculation, except for the zone of secondary flow not reproduced in the inviscid result. The comparison for $M_\infty = 4.0$ is shown in Fig. 15. Generally, the behavior seen here is much like that of the $M_\infty = 1.95$ solution in that the normal extent of the flowfield affected by the wing surface and adjacent vortex is much smaller for the computation than is evident in the experiment. Contours of the turbulent solution practically coincided with those shown in Fig. 15. Finally, Fig. 16 indicates the $M_\infty = 7.0$ comparison. Here the comparison in the outboard region of the wing is good. Along the inboard portion, however, coarseness of the computational domain in the $z$-mesh near the plane of symmetry may account for the lack of agreement between the numerical solution and the experimental data.

## Conclusions and Discussion

Laminar Navier-Stokes solutions have been generated in order to describe the flowfield about a thin delta wing of low aspect ratio for subsonic, sonic, and supersonic leading-edge flow. In the subsonic case, the simulation was seen to reproduce commonly observed physical features including secondary vortex motion, which was not predicted when the flow was assumed to be conical. A corresponding Euler solution for the case appeared to capture the dominant physical behavior of the flowfied. In particular, the surface pressure distribution was well approximated and resulted in a discrepancy in the lift coefficient of less than 7% when compared to the Navier-Stokes solution. For a sonic leading edge, the primary vortex was found to be much smaller in extent and located further inboard than in the subsonic case. Due to the higher streamwise velocity near the surface in this case, no secondary flow evolved. Comparison of this result with a turbulent solution indicated only minor differences

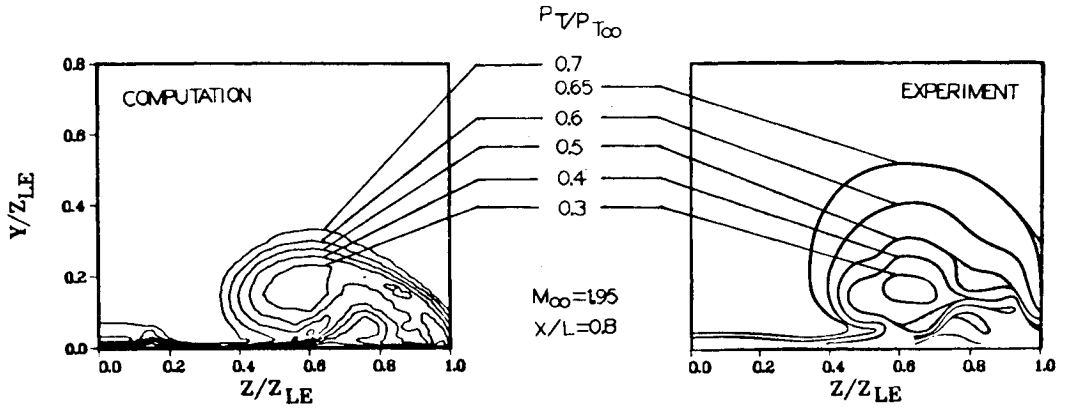


Fig. 14 Comparison of Navier-Stokes total pressure contours above the upper surface with experimental data for $M_\infty = 1.95$ at $x/L = 0.8$.

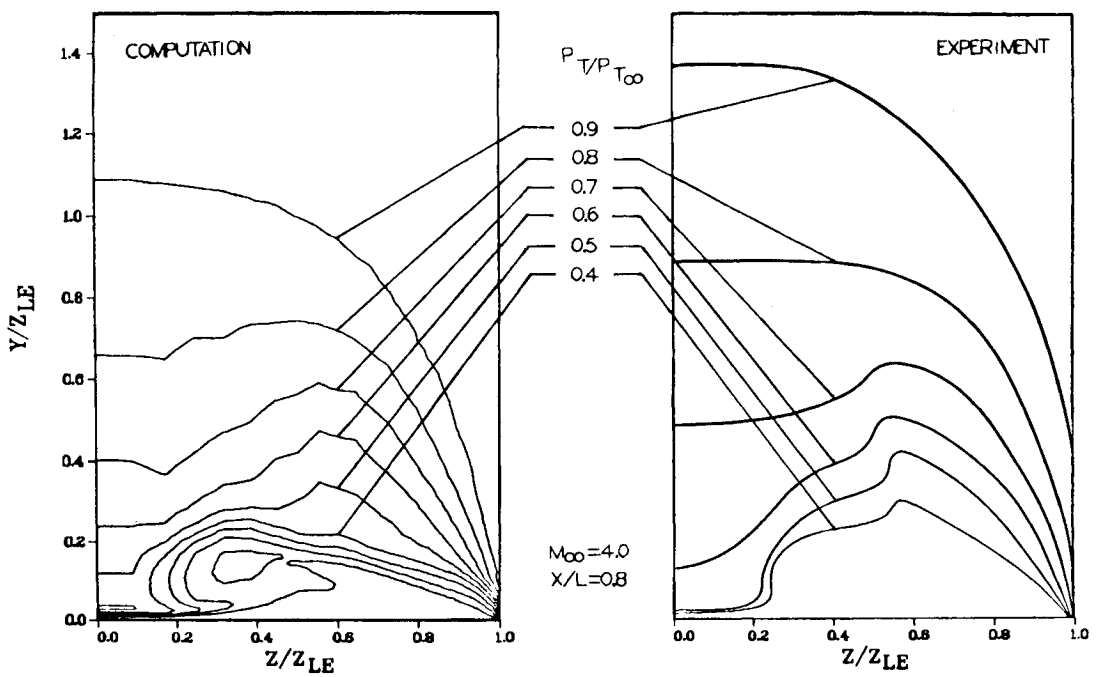


Fig. 15 Comparison of Navier-Stokes total pressure contours above the upper surface with experimental data for $M_\infty = 4.0$ at $x/L = 0.8$.

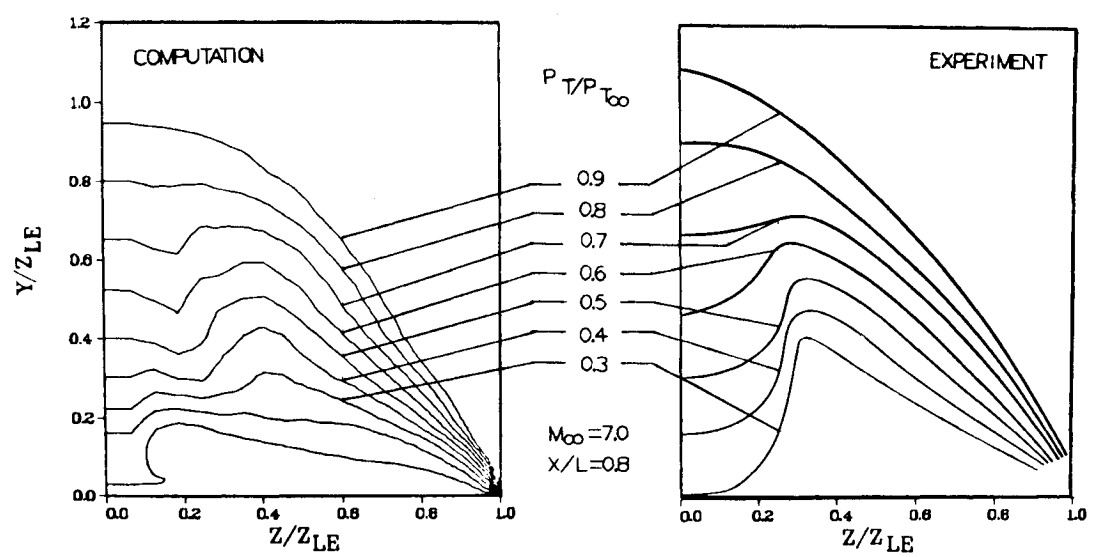


Fig. 16 Comparison of Navier-Stokes total pressure contours above the upper surface with experimental data for $M_\infty = 7.0$ at $x/L = 0.8$.

between the two calculations. When the leading edge was supersonic, separation was found to occur inboard of the leading edge and resulted in a single vortex that was very weak and located near the plane of symmetry. Comparison with experimental data has been made for all three flow regimes. At the two highest Mach numbers, numerical solutions duplicated the upper surface experimental static pressure distributions. Contours of total pressure above the wing upper surface for the numerical results were found to agree qualitatively with the data, but quantitatively the comparison was not good.

Although the Reynolds numbers of the experiments considered here are quite high, it is believed that the calculated laminar solutions provided a good representation of the physical situation. Much of the flow near the surface is directed in an outboard direction (see Fig. 6) with velocities smaller than those occurring streamwise. Thus, a representative Reynolds number based upon cross-plane quantities would be considerably lower than the nominal value, hence justifying laminar flow conditions.

While the solutions presented here have provided insight into the vortex structure for flow over delta wings with sharp leading edges, several additional aspects require further investigation. The effect of a downstream wake, which can be neglected for supersonic freestream conditions at small angles of attack, may have significant impact upon the vortex structure for low-speed flows. At higher angles of attack, the adverse pressure gradient near the trailing edge of the wing may provoke vortex breakdown. Simulation of this phenomenon poses an interesting and challenging future undertaking.

## Acknowledgments

Computational time for the work presented here was provided through the auspices of the Air Force Weapons Laboratory, Kirtland, AFB. In particular, the authors are grateful to J. D. Waskiewicz of AFWL for his help in securing these resources. We also wish to acknowledge W. L. Hankey for several helpful discussions.

## References

[1]Thomann, H., "Measurements of Heat Transfer, Recovery Temperature, and Pressure Distribution on Delta Wings at M = 3," FFA Rept. 93, 1963.

[2]Stanbrook, A. and Squire, L. C., "Possible Types of Flow at Swept Leading Edges," *Aeronautical Quarterly*, Vol. 15, Pt. 1, Feb. 1964, pp. 72-82.

[3]Monnerie, B. and Werle, H., "Study of Supersonic and Hypersonic Flow About a Slender Wing at an Angle of Attack," *Hypersonic Boundary Layers and Flow Fields*, AGARD CP-30, May 1968, (in French), pp. 23-1—23-19.

[4]Narayan, K. Y., "Leeside Flowfield and Heat Transfer of a Delta Wing at $M_\infty = 10$," *AIAA Journal*, Vol. 16, Feb. 1978, pp. 160-165.

[5]Hummel, D., "On the Vortex Formation Over a Slender Wing at Large Angles of Incidence," *High Angle of Attack Aerodynamics*, AGARD CP-247, 1978, pp. 13-1—13-17.

[6]Brown, C. E. and Michael, W. H., "Effect of Leading Edge Separation on the Lift of a Delta Wing," *Journal of the Aeronautical Sciences*, Vol. 21, Oct. 1954, pp. 690-706.

[7]Hall, M. G., "A Theory for the Core of a Leading Edge Vortex," *Journal of Fluid Mechanics*, Vol. 11, Pt. 2, Sept. 1961, pp. 209-228.

[8]Squire, L. C., "The Estimation of Non-Linear Lift of Delta Wings at Supersonic Speeds," *Journal of the Royal Aeronautical Society*, Vol. 67, 1963, pp. 476-480.

[9]Polhamus, E. C., "A Concept of the Vortex Lift of Sharp-Edge Delta Wings Based on a Leading Edge Suction Analogy," NASA TN D-3767, 1966.

[10]Weber, J. A., Brune, G. W., Johnson, F. T., Lu, P., and Rubbert, P. E., "Three-Dimensional Solution of Flows over Wings with Leading-Edge Vortex Separation," *AIAA Journal*, Vol. 14, April 1976, pp. 519-525.

[11]Levin, D. and Katz, J., "Vortex-Lattice Method for the Calculation of the Nonsteady Separated Flow over Delta Wings," *Journal of Aircraft*, Vol. 18, Dec. 1981, pp. 1032-1037.

[12]Klopfer, G. H. and Nielsen, J. N., "Euler Solutions for Wing and Wing-Body Combination at Supersonic Speeds with Leading-Edge Separation," AIAA Paper 80-0126, Jan. 1980.

[13]Erikson, L. E. and Rizzi, A., "Comparison of Vortex Flow Around Wings Using the Euler Equations," *Proceedings of Fourth GAMM Conference on Numerical Methods in Fluid Mechanics, Notes on Numerical Fluid Mechanics*, Academic Press, Vol. 5, 1981, pp. 137-148.

[14]Hitzel, S. M. and Schmidt, W., "Slender Wings with Leading-Edge Vortex Separation—A Challenge for Panel-Methods and Euler Codes," AIAA Paper 83-0562, Jan. 1983.

[15]Vigneron, Y. C., Rakich, J. V., and Tannehill, J. C., "Calculation of Supersonic Viscous Flow over Delta Wings with Sharp Subsonic Leading Edges," AIAA Paper 78-1137, July 1978.

[16]Bluford, G. S., "Numerical Solution of the Supersonic and Hypersonic Viscous Flow around Thin Delta Wings," *AIAA Journal*, Vol. 17, Sept. 1979, pp. 942-949.

[17]Tannehill, J. C., Venkatapathy, E., and Rakich, J. V., "Numerical Solution of Supersonic Viscous Flow over Blunt Delta Wings," AIAA Paper 81-0049, Jan. 1981.

[18]Krause, E., Shi, X. G., and Hartwich, P. M., "Computation of Leading Edge Vortices," AIAA Paper 83-1907, July 1983.

[19]Fujii, K. and Kutler, P., "Numerical Simulation of the Leading-Edge Separation Vortex for a Wing and Strake Wing Configuration," AIAA Paper 83-1908, July 1983.

[20]Shang, J. S., Bunning, P. G., Hankey, W. L., and Wirth, M. C., "Performance of a Vectorized Three-Dimensional Navier-Stokes Code on a CRAY-1 Computer," *AIAA Journal*, Vol. 18, Sept. 1980, pp. 1073-1079.

[21]Baldwin, B. S. and Lomax, H., "Thin Layer Approximation and Algebraic Model for Separated Turbulent Flows," AIAA Paper 78-257, Jan. 1978.

[22]MacCormack, R. W., "The Effect of Viscosity in Hypervelocity Impact Cratering," AIAA Paper 69-354, April 1969.

[23]MacCormack, R. W. and Baldwin, B. S., "A Numerical Method for Solving the Navier-Stokes Equations with Application to Shock-Boundary Layer Interactions," AIAA Paper 75-1, Jan. 1975.